



*Research article*

## **C<sub>60</sub> and Sc<sub>3</sub>N@C<sub>80</sub>(TMB-PPO) derivatives as constituents of singlet oxygen generating, thiol-ene polymer nanocomposites**

**Emily M. Barker, Ashli R. Toles, Kyle A. Guess, and Janice Paige Buchanan \***

Department of Chemistry and Biochemistry, University of Southern Mississippi, 118 College Drive, Hattiesburg, MS 39046, USA

\* **Correspondence:** Email: [paige.buchanan@usm.edu](mailto:paige.buchanan@usm.edu); Tel: +1-601-266-4083;  
Fax: +1-601-266-6075.

**Abstract:** Numerous functionalization methods have been employed to increase the solubility, and therefore, the processability of fullerenes in composite structures, and of these radical addition reactions continue to be an important methodology. C<sub>60</sub> and Sc<sub>3</sub>N@C<sub>80</sub> derivatives were prepared via radical addition of the photodecomposition products from the commercial photoinitiator TMB-PPO, yielding C<sub>60</sub>(TMB-PPO)<sub>5</sub> and Sc<sub>3</sub>N@C<sub>80</sub>(TMB-PPO)<sub>3</sub> as preferred soluble derivatives obtained in high yields. Characterization of the mixture of isomers using standard techniques suggests an overall 1PPO:6TMB ratio of addends, reflecting the increased reactivity of the carbon radical. Although, a higher percentage of PPO is observed in the Sc<sub>3</sub>N@C<sub>80</sub>(TMB-PPO)<sub>3</sub> population, perhaps due to reverse electronic requirements of the substrate. Visually dispersed thiol-ene nanocomposites with low extractables were prepared using two monomer compositions (PETMP:TTT and TMPMP:TMPDE) with increasing fullerene derivative loading to probe network structure-property relationships. Thermal stability of the derivatives and the resulting networks decreased with increased functionality and at high fullerene loadings, respectively. TMPMP:TMPDE composite networks show well-dispersed derivatives via TEM imaging, and increasing *T<sub>g</sub>*'s with fullerene loading, as expected for the incorporation of a more rigid network component. PETMP:TTT composites show phase separation in TEM, which is supported by the observed *T<sub>g</sub>*'s. Singlet oxygen generation of the derivatives decreases with increased functionality; however, this is compensated for by the tremendous increase in solubility in organic solvents and miscibility with monomers. Most importantly, singlet oxygen generation from the composites increased with fullerene derivative loading, with good photostability of the networks.

**Keywords:** fullerenes; C<sub>60</sub>; Sc<sub>3</sub>N@C<sub>80</sub>; fullerene derivatives; thiol-ene; nanocomposites

## 1. Introduction

The use of fullerenes in polymer films and composites has become increasingly popular due to their ability to produce singlet oxygen [1], as well as their unique optical [2–5], magnetic [6,7], electronic [8,9,10], physical [11], and photophysical [1,12,13,14] properties. Though fullerenes have many potential uses, as-prepared, they are completely insoluble in aqueous solutions and only sparingly soluble in common organic solvents, monomers, and polymers, greatly limiting their utility. Fortunately, chemical modification of fullerenes may greatly enhance solubility and processability, thereby leading to a practical realization of many of these unique attributes [15,16]. As a result, a library of reactions has evolved which enable the surface functionalization of fullerenes creating interesting derivatives, which are more amenable to the preparation of fullerene polymer nanocomposites.

Of these, free-radical reactions continue to be an important methodology for the functionalization of fullerenes. The phrase “radical sponge” is often used to emphasize the high radical scavenging activity that  $C_{60}$  exhibits due to the combination of a favorable electron affinity (ca. 2.7–2.8 eV) and large number (30) of conjugated double bonds, which can readily react with radicals.[17] The addition of 11 phenyl groups, 15 benzyl groups, and 34 methyl groups are among the first examples of radical additions to  $C_{60}$  [18,19,20]. A review by Tzirakis et al. [18] summarizes the radical addition of C-, Si-, O-, S-, P-, N-, and metal- centered radicals as well as hydrogen and halogen radicals to fullerenes. In addition, select phosphorylated fullerene derivatives have been shown to possess biological activities [21,22] and optical properties [23,24]. Directly related to this work,  $C_{60}$  was also shown to readily react with commercial initiators such as 2,2'-azobisisobutyronitrile (AIBN), which was discovered during the free-radical polymerization of methyl methacrylate (MMA) and styrene in the presence of  $C_{60}$  [25]. Ford et al. [26] later demonstrated the high reactivity of  $C_{60}$  with other thermal initiators, such as dimethyl azobisisobutyrate (DMAIB).

Compared to empty cage fullerenes, such as  $C_{60}$ , functionalization of  $Sc_3N@C_{80}$ , a  $C_{80}$  cage encapsulating a  $Sc_3N$  complex within, can be less straightforward. A stabilizing effect due to the electrostatic relationship between the  $Sc_3N$  cluster and the  $C_{80}$  cage exists, and the electronic structure of  $[Sc_3N]^{6+}@[C_{80}]^{6-}$  results in a reduced reactivity in most reactions common to the derivatization of  $C_{60}$ , whose reactivity can be compared to an electron-deficient alkene. Although numerous radical additions are successful with  $C_{60}$ , only a few radical additions of metallic nitride fullerenes (MNFs), such as  $Sc_3N@C_{80}$ , have been documented [27–30]. In 2007, Shustova et al. [30] derivatized  $Sc_3N@C_{80}$  via radical addition of  $CF_3$ . Later, Shu et al. [29] derivatized  $Sc_3N@C_{80}$  with carbon-centered radicals generated from diethyl malonate catalyzed by manganese (III) acetate. Shu et al. [28] also demonstrated the reaction of  $Sc_3N@C_{80}$  with photochemically generated benzyl radicals producing a benzyl adduct,  $Sc_3N@C_{80}(CH_2C_6H_5)_2$ , in 82% yield. To a large extent, chemical reactivity is believed to be controlled by the identity of the metal encapsulated, as discussed in a recent report by Echegoyen et al. [31], where the  $Y_3N@C_{80}$ -diethyl malonate monoadduct was successfully prepared under conditions which would not produce the comparable  $Sc_3N@C_{80}$  adduct. This difference in chemical reactivity was attributed to the encapsulated cluster, which affected the reactivity and the regiochemistry of the addition.

Numerous functionalization methods have been employed to increase the solubility, and therefore, the processability of fullerenes. An important breakthrough in polymer photovoltaics was

achieved upon functionalizing pristine C<sub>60</sub>, yielding phenyl-C<sub>61</sub>-butyric acid methyl ester (PCBM), which exhibits enhanced solubility (~50 mg mL<sup>-1</sup> in chlorobenzene) compared to pristine C<sub>60</sub> [32]. In 2009, Troshin et al. [33] prepared various C<sub>60</sub> and C<sub>70</sub> methanofullerenes closely resembling the structure of PCBM to determine structure-property relationships as a function of functionality. The solubilities of the resulting methanofullerenes was found to vary greatly, ranging from 4 mg mL<sup>-1</sup> to ~130 mg mL<sup>-1</sup>, however, a correlation between functionality and solubility was not determined. Furthermore, both empty cage fullerenes and MNFs have been highly hydroxylated yielding water soluble fullerols exhibiting biological activity [34–38] and radical-scavenging ability [39–43] with negligible toxicity [44,45]. Therefore, fullerols have attracted much attention for their use in medical and cosmetic applications.

Specific to this work, fullerenes and their derivatives are also well-known photosensitizers due to their unique electronic  $\pi$ -system [1,5,46,47]. The use of C<sub>60</sub> fullerene as a photosensitizer to generate singlet oxygen as well as C<sub>60</sub>'s photophysical properties have been well documented [1,12,14,48–51]. Upon irradiation the fullerene is converted to an excited triplet state through intersystem crossing. The excited fullerene triplet can then react directly with molecular oxygen via energy transfer generating singlet oxygen, a highly reactive form of molecular oxygen. Once generated, singlet oxygen can be used in a variety of organic reactions such as the ene reaction and the Diels-Alder reaction [52,53]. The ability of a few fullerene derivatives to produce singlet oxygen has also been explored, where singlet oxygen production was found to decrease with an increase in the number addends bound to the cage but was independent of addend functionality [46,54,55,56]. Functionalized fullerenes that generate singlet oxygen have been exploited for their use in biological applications such as photodynamic therapy and antimicrobial coatings [55,57].

In order to utilize the unique properties of fullerenes, many efforts have been made to incorporate fullerenes and fullerene derivatives into a polymer matrix via covalent linkages or blending. Polymer blends and cross-linked networks containing various fullerenes show great promise in the applications of optoelectronic devices, energy conversion systems, magnetic resonance imaging (MRI) contrast agents, photovoltaic devices, oxygen sensors, and as antimicrobial and decontaminating agents [3,51,58,59]. Recently, singlet oxygen generating fullerenes have been utilized as polymer constituents to create stimuli-responsive adhesives and antimicrobial coatings [51,60]. It has been demonstrated that the adhesive properties of rubber-based elastomeric adhesives can be affected when blended with singlet oxygen generators, such as fullerenes, by utilizing a singlet oxygen mediated crosslinking reaction [60]. Singlet oxygen generating fullerenes have also been exploited as potential self-decontaminating agents due to singlet oxygen's ability to react with olefins, dienes, aromatics, peptides, and sulfur atoms, which are found in chemical warfare agents [61]. To date, fullerenes have been incorporated into polymer architectures including polystyrene (PS) [62,63], polyurethanes [61,64,65], and poly(methyl) methacrylate (PMMA) [66]. However, the work herein, evaluates the potential for incorporation of select C<sub>60</sub> and Sc<sub>3</sub>N@C<sub>80</sub> fullerene derivatives into a thiol-ene polymer matrix, which is a relatively new area of research. Thiol-ene networks are inherently a good model matrix due to its well-defined network, possessing narrow glass transition temperatures, which allow us to probe subtle physical changes, such as enthalpic relaxation, photodegradation, network free volume, molecular weight between crosslinks, and elasticity of the network [67,68,69].

Thiol-ene photopolymerizations occur rapidly through a step growth radical polymerization

reaction, do not require solvents for processing, produce optically clear products, and exhibit good thermal and mechanical properties [68,69]. The uniformly structured networks of thiol-ene films allows tuning of properties depending upon the chemical structures of the thiols and enes. Furthermore, thiol-ene photopolymerizations are unique in that they are not inhibited by oxygen and may be polymerizable without the addition of photoinitiators [69,70]. The rate of polymerization of the thiol-ene reaction is directly related to the resulting electron density of the ene, where ene reactivity generally decreases with decreasing electron density. Therefore, electron rich enes polymerize much faster than electron poor enes [69,71,72]. The rate of polymerization of thiols can be affected by inductive resonance; therefore, propionate esters react faster than glycolate esters and both propionate and glycolate esters react much faster than alkyl thiols [69].

The incorporation of fullerenes into thiol-ene composite materials has not been widely studied, and little is known about the consequences of incorporating singlet oxygen generating species into these polymer nanocomposites. Our group's interest lies in the preparation of novel fullerene derivatives as additives to thiol-ene composites and the characterization of the resulting networks. Derivatization of  $C_{60}$  and  $Sc_3N@C_{80}$  with P- and C-centered radicals, resulting from the photochemical decomposition of bis(2,4,6-trimethylbenzoyl)-phenylphosphineoxide (TMB-PPO), was investigated as a function of  $C_{60}$  to TMB:PPO molar ratios. Fullerene derivatives possessing greatly enhanced solubilities were produced and incorporated into thiol-ene nanocomposites at various percent loadings. To our knowledge, this is the first report of functionalizing  $Sc_3N@C_{80}$  with a phosphorous ligand.

## 2. Materials and Method

### 2.1. Materials

Trimethylolpropane diallyl ether (TMPDE) (90%), 1,3,5-triallyl-1,3,5-triazine-2,4,6(1H,3H,5H)-trione (TTT) (98%), trimethylolpropane tris (3-mercaptopropionate) (TMPMP) (>95%), pentaerythritol tetrakis (3-mercaptopropionate) (PETMP) (>95%), 2,2'-azobisisobutyronitrile (AIBN, 98%), benzene (99%), chloroform (>99.8%), dichloromethane (DCM) (>99.5%), methanol (MeOH) (>99.8%), ethanol (EtOH) (>99.5%), acetone (>99.5%), and chloroform-d (99.8% atom D) were obtained from the Sigma Aldrich Chemical Company (St. Louis, MO). Bis(2,4,6-trimethylbenzoyl)-phenylphosphineoxide (TMB-PPO) was purchased from Ciba Specialty Chemicals.  $C_{60}$  (99.6%) and  $Sc_3N@C_{80}$  (MNF) (95%) fullerenes were obtained from SES Research (Houston, TX). All chemicals were used as received.

### 2.2. Preparation of Fullerene Derivatives

$C_{60}$  (75 mg, 104.2  $\mu$ mol) and TMB-PPO (261 mg, 624.4  $\mu$ mol) were added to benzene (150 mL) and sonicated until dissolved, as determined by a resulting clear purple-red solution. The solution was placed in a rayonet photochemical reactor containing sixteen, 350 nm  $\lambda_{max}$  bulbs for 1 hr, at which time a precipitate forms. The resulting dark brown heterogeneous solution was concentrated under reduced pressure. Methanol (100 mL) was then added to the concentrated sample to dissolve any unreacted TMB-PPO from the precipitate of brown solids. The precipitate was separated via filtration using a 0.45  $\mu$ m nylon filter membrane, followed by drying at 50 °C overnight to give

$C_{60}(\text{TMB-PPO})_x$  in crude isolated yields of ~95%. Further purification was afforded via multiple passes on a gravity chromatography column (silica gel- SiliCycle® 40–63  $\mu\text{m}$ ), using a gradient solvent mixture from 100% DCM to 10% MeOH/90% DCM. A coffee colored narrow band was isolated and vacuum oven dried at 50 °C overnight to yield black crystals in 80% recovered yield. A similar method was utilized to prepare  $\text{Sc}_3\text{N}@C_{80}(\text{TMB-PPO})_y$  derivatives.  $\text{Sc}_3\text{N}@C_{80}$  (5 mg, 4.5  $\mu\text{mol}$ ) and TMB-PPO (11.5 mg, 27.5  $\mu\text{mol}$ ) were added to benzene (100 mL), sonicated, and placed in the rayonet photoreactor for 1 hr. The resulting tan heterogeneous solution was then filtered using a 0.45  $\mu\text{m}$  nylon filter membrane. Solids were washed 3x with additional benzene (100 mL) to remove unreacted  $\text{Sc}_3\text{N}@C_{80}$  and TMB-PPO starting materials, followed by drying at 50 °C overnight to give  $\text{Sc}_3\text{N}@C_{80}(\text{TMB-PPO})_3$  in crude isolated yields of ~ 95%. The purified fullerene derivatives were characterized via thermogravimetric analysis (TGA), FTIR spectroscopy, and MALDI.

### 2.3. Preparation of Fullerene-Containing Thiol-Ene Nanocomposites

Fullerene containing thiol-ene (TE) films were prepared by adding a known mass of the  $C_{60}(\text{TMB-PPO})_5$  derivative to a TE monomer mix of either PETMP:TTT or TMPMP:TMPDE monomers at varying TE monomer concentrations of 1:1 to 1:0.75 molar equivalents. AIBN thermal initiator (1 wt% solids) was added to the sample, and the resulting mixture was combined in a high shear mixer (FlackTec Inc SpeedMixer™) at 2,400 rpm for 5 min. DCM (2–10 mL) was added to the sample to aid in uniform mixing. Any residual solvent was removed under reduced pressure, and the resulting clear sample was added to a 10 g Teflon release mold and placed in a 50–65 °C oven for at least 24 hrs to ensure complete polymerization. A similar method was utilized for the incorporation of  $\text{Sc}_3\text{N}@C_{80}(\text{TMB-PPO})_3$  into the TE film.  $\text{Sc}_3\text{N}@C_{80}(\text{TMB-PPO})_3$  (1.5 wt%) was added to TMPMP:TMPDE monomer mix prepared using a 1:0.75 molar ratio of thiol and ene. AIBN and acetone (~20 mL) were added to the sample, which was then mixed under high shear. Residual solvent was removed, and the concentrated sample was added to a Teflon release mold and placed in a 65–85 °C oven until fully cured. Five different sets of fullerene-TE films were prepared:  $C_{60}(\text{TMB-PPO})_5$  films prepared using PETMP:TTT and TMPMP:TMPDE monomers at 1:1 and at 1:0.75 molar equivalents at five different loadings of  $C_{60}$  (0, 1, 5, 10, and 20 wt%) and a  $\text{Sc}_3\text{N}@C_{80}(\text{TMB-PPO})_3$  film using TMPMP:TMPDE monomers at 1:0.75 molar equivalents with a  $\text{Sc}_3\text{N}@C_{80}(\text{TMB-PPO})_3$  loading of 1.5 wt % for a total of 21 films.

### 2.4. Characterization

#### 2.4.1. Thermogravimetric Analysis (TGA)

The thermal stability of the prepared fullerene derivatives and fullerene-TE nanocomposites were evaluated using a TA instruments Q500 series thermogravimetric analysis (TGA) instrument by monitoring change in weight as a function of temperature under nitrogen. The samples (~ 10 mg) were analyzed in aluminum pans over the temperature range of 25–600 °C at a heating rate of 10 °C/min. The number of addends attached to the fullerene cage was estimated by calculating the ratio of the weight loss at 115–570 °C to the weight loss at temperatures above 570 °C [73]. The thermal degradation onset temperature was reported as the temperature corresponding to 10% mass loss.

#### 2.4.2. Solubility Studies

The solubility of  $C_{60}(\text{TMB-PPO})_x$  in common solvents was determined using a method adapted from Troshin et al.[33] In general, saturated solutions of the fullerene derivatives were prepared by mixing an excess amount of fullerene derivative (>25 mg) in 1 mL solvent (MeOH, EtOH, acetone, DCM, chloroform, and benzene) at room temperature (~25 °C) for 24 hrs. Following mixing, the prepared saturated solutions were filtered using 0.25  $\mu\text{m}$  PTFE syringe filters into a glass vial of known mass, and solvent was removed at 50 °C under reduced pressure.

#### 2.4.3. FT-IR, $^1\text{H-NMR}$ , Elemental Analysis (EA), and Mass Spectrometry (MS), and XPS

Fourier transform infrared spectroscopy (FT-IR) analysis was performed in the 500–4000  $\text{cm}^{-1}$  range using a Nicolet Nexus 470 FT-IR spectrometer equipped with a diamond crystal ATR accessory.  $^1\text{H-NMR}$  spectrums were obtained using a Bruker 400 MHz NMR in chloroform-d, and all shifts are reported relative to chloroform-d at 7.24 ppm. Vacuum dried samples (50 °C for 48 hrs) were sent to a commercial analytical company, Galbraith Laboratories Inc. (Knoxville, TN) for elemental analysis. Matrix-Assisted Laser Desorption/Ionization MALDI-MS of  $C_{60}(\text{TMB-PPO})_5$  and  $\text{Sc}_3\text{N}@C_{80}(\text{TMB-PPO})_3$  was obtained using a MicroFlex Bruker mass spectrometer with a laser power of ~90%. The matrix was prepared by dissolving 2,5-dihydroxybenzoic acid (1 mg) in 1 mL of a mixed solvent of 0.1% trifluoroacetic acid (TFA)/DCM (1:2, v/v). The  $C_{60}(\text{TMB-PPO})_5$  adduct (1 mg/mL), dissolved in DCM, was premixed with the prepared matrix at a 1:2000 molar analyte-to-matrix ratio, then applied to the target plate, followed by solvent evaporation. A ProteoMass<sup>TM</sup> mix containing bradykinin fragment 1–7 (757.3997 Da), angiotensin II (human) (1,046.5423 Da), and insulin (bovine) (5,730.6087 Da), dissolved in acetonitrile, was used as references. Digested samples were sent to a commercial analytic company, Bonner Analytical Testing Co. (Hattiesburg, MS) for inductively-coupled plasma mass spectrometry (ICP-MS). Prior to ICP-MS analysis, a known mass of sample (~1.5 mg) was added to a digestion tube containing concentrated sulfuric acid (3.5 mL) and  $\text{H}_2\text{O}_2$  (30 %, 3.5 mL). The resulting mixture was heated to 200 °C until no solids were visual and solutions were clear (~6 hrs). Upon cooling to room temperature, resulting solutions were filtered using 0.2  $\mu\text{m}$  PTFE syringe filters and diluted with water yielding a 50 mL sample. X-ray photoelectron spectroscopy (XPS) analysis was performed at the Naval Research Laboratory (NRL) (Washington, DC) using a Thermo Scientific K-Alpha X-ray photoelectron spectrometer equipped with monochromatic Al  $K\alpha$  radiation. Survey spectra were acquired from –10 to 1350 eV with 200.00 eV pass energy, 25 ms dwell time, and 1.000 eV step size. High resolution elemental scans were performed for C 1s, N 1s, O 1s, P 2p, and Sc 2p. 10 scans were collected and averaged for C, N, and O, while 30 scans were averaged for P 2p. Each scan employed 30 eV pass energy, 50 ms dwell time, and 0.150 eV step size. Peak fitting and integration were performed via Smart Fitting on Advantage XPS software.

#### 2.4.4. Singlet Oxygen Studies

Direct singlet oxygen solution based studies were performed using a method adapted by Barker et al. [74]  $C_{60}(\text{TMB-PPO})_x$  (100  $\mu\text{mol}$ ) samples were prepared by dissolving  $C_{60}(\text{TMB-PPO})_x$  in benzene and sonicating for 5 min or until fully dissolved. Benzene (2 mL) was added to a

fluorometer cuvette with a septum cap and stir bar, and then 10  $\mu\text{L}$  of the prepared sample was added to the cuvette via microsyringe. The resulting sample was then excited at 350 nm, and an emission scan was obtained from 1200–1350 nm. Any singlet oxygen produced was directly detected via the phosphorescence of singlet oxygen at 1270 nm using a Photon Technology International (PTI) FeliX32 InGaAs-TE photodiode with pre-amplifier NIR detector. Following each emission scan obtained, more sample (10–100  $\mu\text{L}$ ) was added to the cuvette to obtain calibration curves. Analogous methods were employed to obtain a calibration curve for the singlet oxygen generation of pure  $\text{C}_{60}$  (10  $\mu\text{M}$ ) for comparison.

Thin films for singlet oxygen studies were prepared by coating Teflon containers with prepared TMPMP:TMPDE monomer mix containing  $\text{C}_{60}(\text{TMB-PPO})_5$  (1 and 10 wt%  $\text{C}_{60}$ ) or 1.5 wt%  $\text{Sc}_3\text{N}@\text{C}_{80}(\text{TMB-PPO})_3$  and curing at 65  $^\circ\text{C}$  for at least 24 hrs. Films were prepared at different thicknesses to yield similar transparencies for singlet oxygen studies. Resulting films were then adhered to one side of a fluorometer cuvet containing benzene. An excitation scan was obtained from 300–600 nm with the emission set to 1270 nm, and emission scans were obtained from 1200–1350 nm while exciting at 420 nm.

#### 2.4.5. Gel Fractions

Gel fractions of the prepared films were obtained by dissolving a known mass of the film in benzene, allowing the samples to rest at room temperature for 24 hrs, and recovering the remaining film. Residual solvent was removed at 25  $^\circ\text{C}$  under reduced pressure. Gel fractions were recorded as the final mass of the film after solvent removal over the initial mass and is expressed as a percent. UV-Vis was obtained on the resulting solution to determine the amount of extractable  $\text{C}_{60}(\text{TMB-PPO})_5$ , through comparisons to known standards.

#### 2.4.6. Differential Scanning Calorimetry (DSC)

The glass transition temperature ( $T_g$ ) of films was determined using a TA Instruments Q2000 modulated differential scanning calorimetry (DSC). The thermally cured films (~10 mg) were monitored over the temperature range of  $-50$  to 150  $^\circ\text{C}$  in a heat/cool/heat cycle at 5  $^\circ\text{C}/\text{min}$ . The  $T_g$  was obtained from the second heating cycle.

#### 2.4.7. Transmission Electron Microscopy (TEM)

Fullerene-containing TE nanocomposites were analyzed using a Zeiss EM-900 TEM at 50kV. TEM samples were prepared using a Leica EM FC6 ultramicrotome with cryochamber cooled to  $-60$   $^\circ\text{C}$  and sliced using glass knives. Samples were applied to 300 mesh copper grids, purchased from Electron Microscopy Sciences.

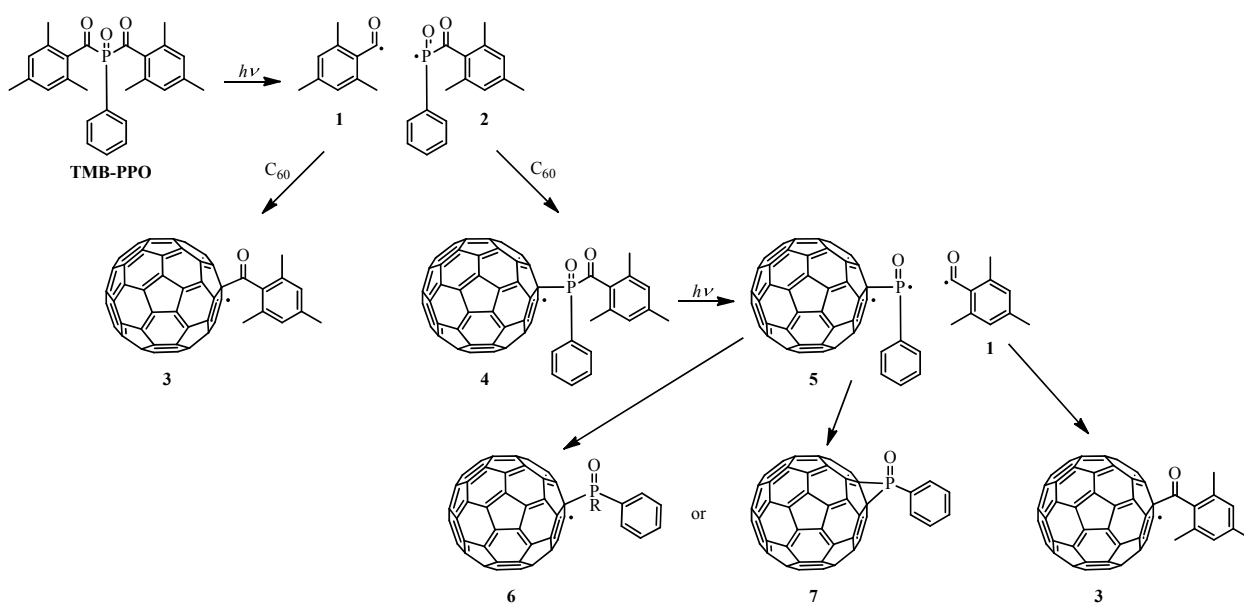
#### 2.4.8. Film Photodegradation Studies

FT-IR samples were prepared for photodegradation studies by diluting the resulting  $\text{C}_{60}(\text{TMB-PPO})_5$  TE monomer mix with DCM, yielding a 10 wt % solid solution. The dilute solution (100  $\mu\text{L}$ ) was then spin casted onto sodium chloride salt plates using an ED101D Digital Photo

Resist Spinner (Headway Research, TX) at 1000 rpm for 60s. Coated salt plates were then placed in a 65 °C oven for at least 48 hrs allowing the films to cure. The concentration of C<sub>60</sub> varied from 0–10 wt%, and irradiation time spanned from 0–4 hrs under a high-pressure mercury-xenon lamp. FT-IR measurements were taken before and after irradiation using a PerkinElmer Spectrum 100 spectrometer in the 450–4000 cm<sup>-1</sup> range.

### 3. Results and Discussion

In general, C<sub>60</sub> and Sc<sub>3</sub>N@C<sub>80</sub> derivatives were prepared via radical addition of the photodecomposition products from the commercial photoinitiator (TMB-PPO), according to Scheme 1. The reaction of C<sub>60</sub> with thermal initiators AIBN and DMAIB has also been reported [25,26]. As illustrated in Scheme 1, both C- and P-centered radicals are produced during photodecomposition, which may either add to C=C or terminate through hydrogen abstraction or coupling reactions [75]. A brief description of the variety of radicals and products that may be produced in Scheme 1 is as follows. TMB-PPO undergoes an initial  $\alpha$ -cleavage yielding a benzoyl (**1**) and an (acyl)phosphinoyl (**2**) radical, both of which may react with C<sub>60</sub> yielding the C<sub>60</sub>-benzoyl radical adduct (**3**) and a C<sub>60</sub>-(acyl)phosphinoyl radical (**4**), respectively. The C<sub>60</sub>-(acyl)phosphinoyl radical (**4**) can undergo a second  $\alpha$ -cleavage forming another benzoyl (**1**) and a C<sub>60</sub>-phosphinoyl radical (**5**). The benzoyl radical (**1**) produced can then react with another C<sub>60</sub>, yielding another C<sub>60</sub>-benzoyl radical adduct (**3**), and the C<sub>60</sub>-phosphinoyl radical (**5**) produced can with undergo hydrogen abstraction yielding product **6** or couple yielding product **7**



**Scheme 1.** Proposed reaction between C<sub>60</sub> and TMB-PPO.

Structure-reactivity relationships based on the number of addends bound to C<sub>60</sub> was determined by varying the molar ratio of C<sub>60</sub> to TMB:PPO. Derivatives prepared during this study and the corresponding fullerene:TMB-PPO molar ratios are reported in Table 1. Using thermogravimetric analysis (TGA), the maximum number of TMB-PPO addends bound to C<sub>60</sub> was found to be five.

Representative TGA plots of fullerene derivatives are provided in Figure 1, including  $C_{60}$ ,  $Sc_3N@C_{80}$ , and TMB-PPO for comparison. The number of addends increases with excess TMB-PPO only to a ratio of  $C_{60}$ :TMB-PPO of 1:6, and above this ratio, higher order adducts were not observed and the isolated yield of soluble products decreased. Therefore, the optimal ratio of 1:6 was chosen for  $Sc_3N@C_{80}$ , which resulted in an  $Sc_3N@C_{80}$  adduct containing three TMB-PPO addends. The thermal degradation onset temperatures of the resulting adducts were also determined from TGA and are reported in Table 1. As expected, the thermal degradation onset temperatures of the resulting adducts fall between 190–236 °C, indicating a slightly elevated thermal stability over TMB-PPO alone (191 °C) but decreases with increasing functionality.

**Table 1.** Derivative functionality and thermal stability as a function of fullerene:TMB-PPO reactivity.

Sample ID	Fullerene:TMB-P PO Molar Ratio <sup>a</sup>	Avg. # Addends <sup>b</sup>	% Yield <sup>c</sup>	Degradation Onset (°C) <sup>d</sup>	% Char <sup>e</sup>
$C_{60}(\text{TMB-PPO})_x$	1:1	2	> 95	236	68
	1:3	3	> 95	208	61
	1:6	5	> 95	199	48
	1:12	5	> 85	-	-
$Sc_3N@C_{80}(\text{TMB-PPO})_3$	1:6	3	> 95	190	63
TMB-PPO	-	-	-	191	1
$C_{60}^f$	-	-	-	642	95
$Sc_3N@C_{80}$	-	-	-	719	93

<sup>a</sup>Using a rayonet photoreactor, samples were irradiated in benzene at 350 nm for 1 hr.; <sup>b</sup>calculated from TGA plots as reported by Singh et al.; <sup>c</sup>isolated yields based on the average molecular mass of the derivative population; <sup>d</sup>calculated from TGA plots as the temperature corresponding to 10% mass loss; <sup>e</sup>% char is reported as the mass remaining above 600 °C from TGA analysis; and <sup>f</sup> $C_{60}$  control.

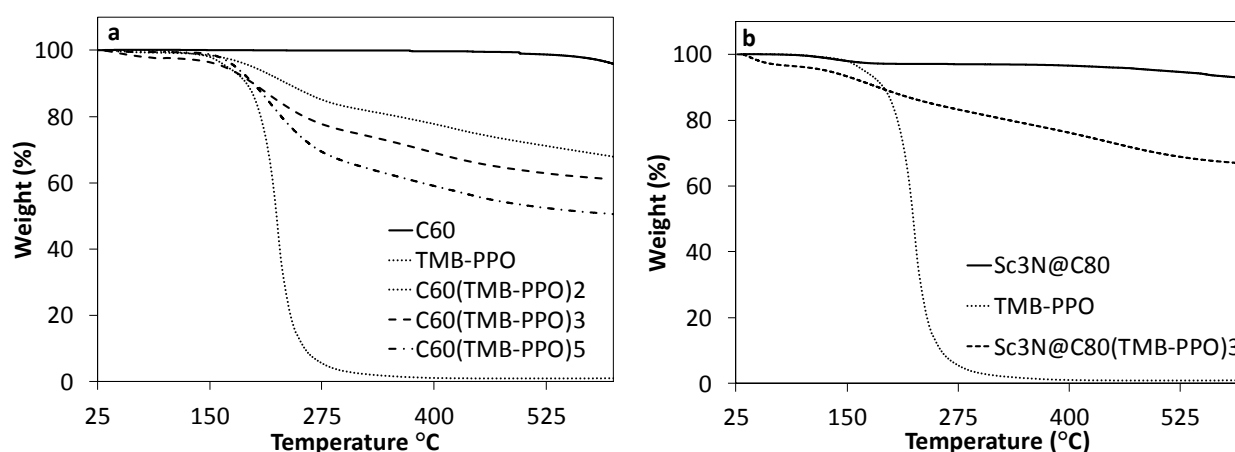


**Figure 1.** Thermal analysis of derivatives and controls: (a) TMB-PPO,  $C_{60}$ , and  $C_{60}(\text{TMB-PPO})_x$  derivatives and (b)  $Sc_3N@C_{80}$  and  $Sc_3N@C_{80}(\text{TMB-PPO})_3$ .

A primary goal of this work was to prepare fullerene derivatives having increased solubility in common organic solvents and miscibility with TE monomers. Solubility studies were performed

using a method adapted from Troshin et al. [33] and are reported in Table 2. The number of TMB-PPO addends bound to C<sub>60</sub> was found to dramatically change the solubility of the adducts. In general, increasing the number of addends resulted in an increase in solubility of the resulting fullerene derivatives. The addition of five TMB-PPO addends was found to increase C<sub>60</sub>'s solubility to a remarkably high value of ~260 mg mL<sup>-1</sup> in DMC. However, the addition of two and three TMB-PPO addends only increased the solubility up to ~18–19 mg mL<sup>-1</sup> also in DMC. The increase in solubility is attributed to the addition of carbonyl and phosphine oxide functional groups, which increase polarity of the derivative.

**Table 2.** Solubility of fullerene derivatives in common solvents at 20 °C reported in mg mL<sup>-1</sup>.

	MeOH	EtOH	Acetone	DCM	CHCl <sub>3</sub>	Benzene
Dielectric constant	33	24.3	21	9.1	4.8	2.28
C <sub>60</sub> [76]	0	0.001	0.001	0.26	0.16	1.7
C <sub>60</sub> (TMB-PPO) <sub>2</sub>	0.2	0.3	0.5	18	14	8
C <sub>60</sub> (TMB-PPO) <sub>3</sub>	0.4	1	1.3	19	15	11
C <sub>60</sub> (TMB-PPO) <sub>5</sub>	6	3	40	260	219	91
Sc <sub>3</sub> N@C <sub>80</sub>	0	0	0	0.1	0.8	1.1
Sc <sub>3</sub> N@C <sub>80</sub> (TMB-PPO) <sub>3</sub>	1.5	1.4	1.3	0	0	0

<sup>a</sup>Average of triplicate measurements, all values within ±10%.

Further characterization was performed on the most soluble derivative of each fullerene, i.e. C<sub>60</sub>(TMB-PPO)<sub>5</sub> and Sc<sub>3</sub>N@C<sub>80</sub>(TMB-PPO)<sub>3</sub>. FT-IR collected on the purified C<sub>60</sub>(TMB-PPO)<sub>5</sub> and Sc<sub>3</sub>N@C<sub>80</sub>(TMB-PPO)<sub>3</sub> samples support the successful attachment of TMB-PPO, through the presence of shifts in characteristic peaks (Supporting Information Figures S1 and S2). An observed shift in the C=O<sub>TMB</sub> from 1680 to 1707 cm<sup>-1</sup> and 1731 cm<sup>-1</sup> is observed for C<sub>60</sub>(TMB-PPO)<sub>5</sub> and Sc<sub>3</sub>N@C<sub>80</sub>(TMB-PPO)<sub>3</sub>, respectively. A comparable shift results in the P=O<sub>PPO</sub> peaks from 1201 and 1222 cm<sup>-1</sup> to 1223 and 1242 cm<sup>-1</sup> for C<sub>60</sub>(TMB-PPO)<sub>5</sub> and 1261 cm<sup>-1</sup> for Sc<sub>3</sub>N@C<sub>80</sub>(TMB-PPO)<sub>3</sub>. MALDI-MS analysis on the C<sub>60</sub>(TMB-PPO)<sub>5</sub> yielded significant peaks at *m/z* 720 and 1386 corresponding to pure C<sub>60</sub> and C<sub>60</sub> with ~5 TMB-PPO addends attached. Sc<sub>3</sub>N@C<sub>80</sub>(TMB-PPO)<sub>3</sub> yielded peaks a *m/z* 1109 corresponding to pure Sc<sub>3</sub>N@C<sub>80</sub>, suggesting loss of functionality during laser ablation which is a common occurrence with fullerene derivatives. (Supporting Information Figures S3 and S4). EA experimental percent compositions of C 78.6, H 4.4, O 15.6, P 1.4 were obtained for C<sub>60</sub>(TMB-PPO)<sub>5</sub> and suggested the attachment of 5 TMB-PPO addends at a ratio of 0.7 PPO to 4.3 TMB (1PPO:6TMB) addends per C<sub>60</sub>, which correlates well with TGA and MALDI. ICP-MS and XPS were obtained for both C<sub>60</sub>(TMB-PPO)<sub>5</sub> and Sc<sub>3</sub>N@C<sub>80</sub>(TMB-PPO)<sub>3</sub>. ICP-MS suggests that 1.6% of the C<sub>60</sub>(TMB-PPO)<sub>5</sub> sample consists of phosphorous, which correlates with elemental analysis. IPC also suggests the binding of ~2.25 phosphorous addends per Sc<sub>3</sub>N@C<sub>80</sub>, where TGA suggested a total of three addends bound to Sc<sub>3</sub>N@C<sub>80</sub> indicating a higher binding of phosphorous to Sc<sub>3</sub>N@C<sub>80</sub> than C<sub>60</sub>. ICP data was also found to correlate well with FT-IR, where

phosphine oxide peaks were stronger than the carbonyl peaks for the  $\text{Sc}_3\text{N}@C_{80}(\text{TMB-PPO})_3$  sample. XPS data, along with FT-IR, suggests the binding of phosphine oxide to  $C_{60}$  and  $\text{Sc}_3\text{N}@C_{80}$ . In summary, shifts in the characteristic TMB-PPO peaks observed in the FT-IR, in combination with MALDI and the increased solubilities, supports the successful derivatization of  $C_{60}$  and  $\text{Sc}_3\text{N}@C_{80}$  with TMB-PPO.

Since the cleavage reactions of TMB-PPO yields a 2:1 ratio of TMB and PPO radicals (Scheme 1), both of which can readily react with  $C_{60}$ ,  $^1\text{H-NMR}$  was performed to determine the relative ratio of TMB and PPO addends bound to  $C_{60}(\text{TMB-PPO})_5$ . As observed in Supporting Information Figure S5, the TMB-PPO starting material possesses well-resolved and unique hydrogen chemical shifts for both TMB ( $H_a$ , 7.86  $\delta$ ;  $H_b$ , 7.53  $\delta$ ;  $H_c$ , 7.40  $\delta$ ) and PPO ( $H_d$ , 6.77  $\delta$ ;  $H_e$ , 2.23  $\delta$ ;  $H_f$ , 2.12 $\delta$ ), allowing for the easy integration of  $^1\text{H-NMR}$  peak areas. Unlike the starting material, the  $C_{60}(\text{TMB-PPO})_5$  adduct yields broad peaks for TMB ( $H_a, H_b, H_c$ , 7.57  $\delta$ ) and PPO ( $H_d, H_e, H_f$ , 2.13  $\delta$ ) addends, which is suggestive of a population of isomers and not a single isomer. However, although broad peaks are present in the  $^1\text{H-NMR}$  spectrum of the  $C_{60}(\text{TMB-PPO})_5$  derivative, regions characteristic of TMB and PPO do not overlap, allowing for successful integration. The relative ratio of TMB to PPO addends was determined by integration and normalizing for the number of hydrogens. The  $^1\text{H-NMR}$  data further supports a ratio of 0.7 PPO to 4.3 TMB (1PPO:6TMB) addends per  $C_{60}$ , which correlates well with EA and ICP-MS.

**Table 3.** Efficiency of singlet oxygen generation by derivatives.

Derivatives	Derivatives ( $\mu\text{M}$ )	$C_{60}$ ( $\mu\text{M}$ )	Relative Efficiency
$\text{Sc}_3\text{N}@C_{80}$	0.3	0.1	-3
$C_{60}(\text{TMB-PPO})_2$	9	0.9	-10
$C_{60}(\text{TMB-PPO})_3$	13	1	-13
$C_{60}(\text{TMB-PPO})_5$	25	1	-25

Singlet oxygen was directly detected via phosphorescence at 1270 nm at  $\lambda_{\text{ex}} = 350$  nm.

Direct singlet oxygen studies were performed using a method previously reported by Barker et al. [74] In general, solution based assays were performed through the direct detection of the singlet oxygen phosphorescence (1270 nm) produced upon exciting a catalytic amount of  $C_{60}(\text{TMB-PPO})_x$  and  $\text{Sc}_3\text{N}@C_{80}(\text{TMB-PPO})_3$  adducts at 350 nm. Emission spectrums were obtained for pristine  $C_{60}$  and  $C_{60}(\text{TMB-PPO})_x$  derivatives to obtain normalized responses yielding  $C_{60}$  equivalent correlation concentrations, which are reported in Table 3 and Supporting Information Figure S6. In general, an expected trend was observed where emission intensity increased with increasing concentration and the generation of singlet oxygen decreased upon increased derivatization of  $C_{60}$ . A previous study by Hamano et al. [46] showed a similar trend where the efficiency of fullerene derivatives to produce singlet oxygen was not dependent on the type of added but was dependent on the number of addends, where efficiency decreased with an increase in functionality. Singlet oxygen studies were also performed on  $\text{Sc}_3\text{N}@C_{80}(\text{TMB-PPO})_3$ . Interestingly, although  $\text{Sc}_3\text{N}@C_{80}$  itself was shown to produce singlet oxygen, derivatization greatly diminished the response in the adduct to below confidence.

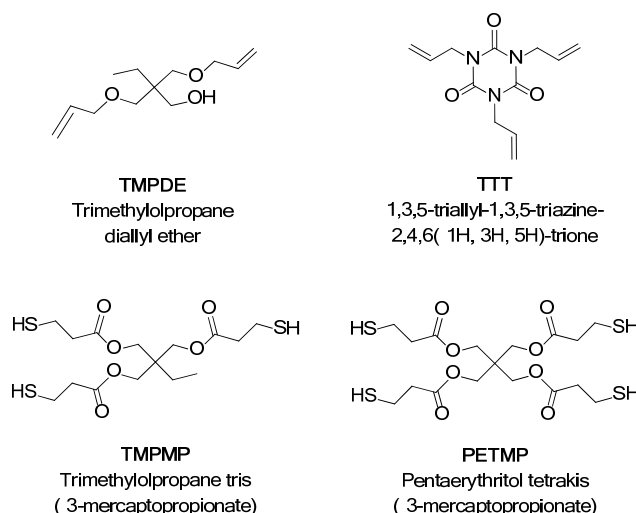
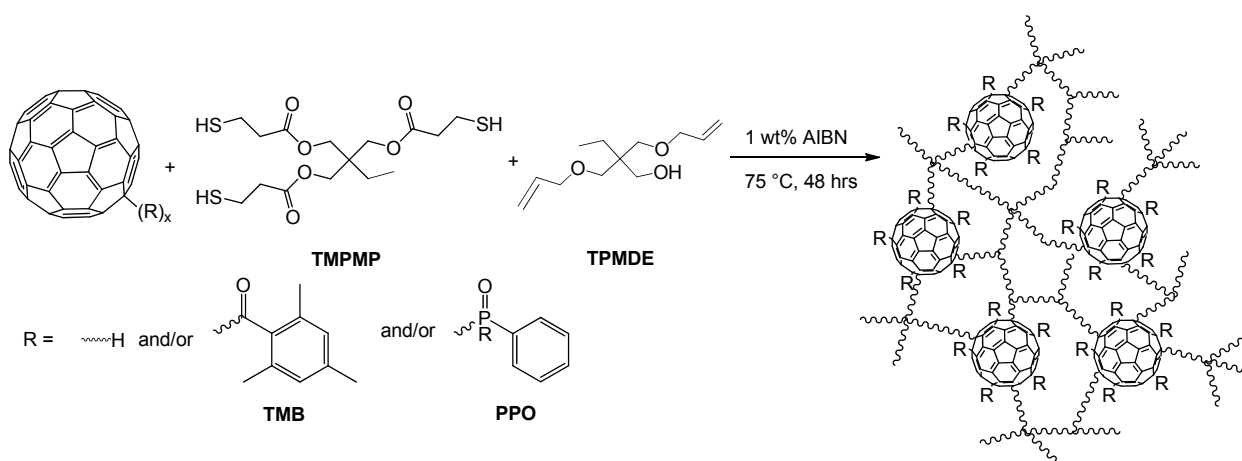


**Figure 2.** Identity and chemical structures of monomers used in the synthesis of fullerene-nanocomposites.

Enhanced solubility in organic media for the derivatives enabled the preparation of fullerene-TE nanocomposites, according to Scheme 2.  $C_{60}(TMB-PPO)_5$  and  $Sc_3N@C_{80}(TMB-PPO)_3$  were added to a TE monomer mix of either PETMP:TTT or TMPMP:TMPDE (Figure 2) at two TE molar equivalents of 1:1 or 1:0.75. The concentration of the ene was reduced in one series in anticipation of fullerene derivatives acting as a reactive ene and capturing radicals generated during the thermal polymerization of the composites. Two monomer compositions were explored, a rigid system, PETMP:TTT ( $T_g$  56), and a flexible system, TMPMP:TMPDE ( $T_g$  -32), to allow a broader scope of structure-property determinations, with regard to thermal and mechanical properties. Five different sets of fullerene-TE films were prepared (Table 4). Representative images of the resulting TE films, placed in order of increasing  $C_{60}$  loading, are provided in Figure 3 and Supporting Information Figures S7–S9.



**Scheme 2.** General preparation of fullerene containing TE nanocomposites.

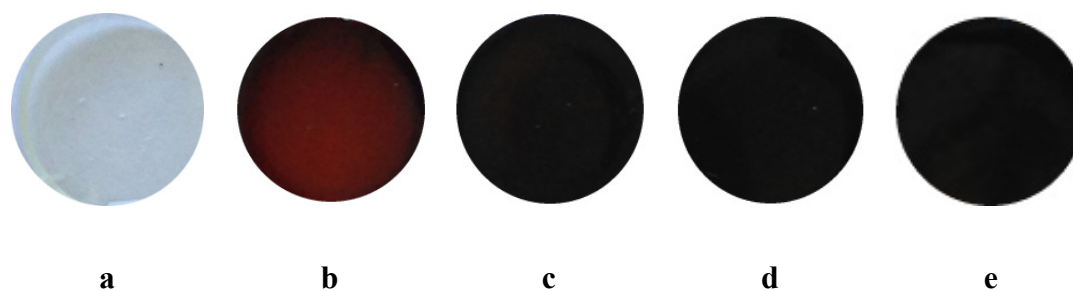


**Figure 3.** Images of  $C_{60}(\text{TMB-PPO})_5$  TMPMP:TMPDE-0.75 at (a) 0%, (b) 1%, (c) 5%, (d) 10%, and (e) 20% equivalent loading of  $C_{60}$ .

**Table 4.** Physical and mechanical analysis of fullerene containing TE nanocomposites.

Monomers/Sample ID <sup>a</sup>	Wt % $C_{60}(\text{TMB-PPO})_5$	Ene/Thiol ratio	Gel %	% Extractable $C_{60}(\text{TMB-PPO})_5$	Glass Transition Temperature ( $T_g$ ) DSC	Thermal Degradation Onset ( $^{\circ}\text{C}$ ) <sup>d</sup>	% Char <sup>e</sup>
PETMP:TTT-1-0	0	1	99	-	56	352	7.2
PETMP:TTT-1-1	2	1	99	0	60	349	8.8
PETMP:TTT-1-5	10	1	99	0	42	339	13.8
PETMP:TTT-1-10	19	1	88	15	19	328	20.5
PETMP:TTT-1-20*	39	1	47*	63*	9*	257	29.6
PETMP:TTT-0.75-0	0	0.75	99	-	31	348	7.7
PETMP:TTT-0.75-1	2	0.75	99	0	38	342	8.9
PETMP:TTT-0.75-5	10	0.75	99	0	41	338	13.8
PETMP:TTT-0.75-10	19	0.75	99	0	41	323	18.2
PETMP:TTT-0.75-20	39	0.75	98	5	33	274	27.7
TMPMP:TMPDE-1-0	0	1	99	-	-32	323	1.4
TMPMP:TMPDE-1-1	2	1	97	1	-28	316	2.9
TMPMP:TMPDE-1-5	10	1	95	2	-25	301	7.3
TMPMP:TMPDE-1-10	19	1	93	3	-20	288	13.3
TMPMP:TMPDE-1-20	39	1	93	7	-5	279	23.4
TMPMP:TMPDE-0.75-0	0	0.75	91	-	-33	335	1.7
TMPMP:TMPDE-0.75-1	2	0.75	99	0	-28	309	3.1
TMPMP:TMPDE-0.75-5	10	0.75	95	2	-27	294	10.1
TMPMP:TMPDE-0.75-10	19	0.75	94	5	-20	293	15.2
TMPMP:TMPDE-0.75-20	39	0.75	93	6	-4	263	28.8
TMPMP:TMPDE-0.75-1.5	2.4	0.75	96	0	-33	296	5.7
$\text{Sc}_3\text{N}@C_{80}$							

<sup>a</sup>Samples identified by monomer composition (PETMP:TTT or TMPMP:TMPDE), ene/thiol ratio (1 or 0.75), and % equivalent loading  $C_{60}$  (0, 1, 5, 10, or 20%).

As seen in Figure 4, the incorporation of  $C_{60}(\text{TMB-PPO})_5$  into the TE films results in a visually more uniform and continuous composition compared to the addition of pure  $C_{60}$ . A general and expected trend was observed, where higher loadings of  $C_{60}$  resulted in increasingly darker films (Figure 3). Curing time was found to be dependent on monomer identity and  $C_{60}$  loading, where curing times increased with an increase in  $C_{60}$  loading and with a decrease in monomer rigidity. We attribute the increased curing times to the persistent radical scavenging ability of fullerenes. Furthermore, the increased curing times for TMPMP:TMPDE compared to the PETMP:TTT monomers is expected due to the lower monomer functionality. A composite was considered cured coincident with the disappearance of the monomer SH and C=C absorptions.



**Figure 4.** Side-by-side comparison of 1 wt%  $C_{60}$  incorporated into a TE matrix using pure  $C_{60}$  (left) and  $C_{60}(\text{TMB-PPO})_5$  (right).

The gel percents and extractable  $C_{60}(\text{TMB-PPO})_5$  from the composites were analyzed to assess the nature and degree of incorporation of the derivatives. As seen in Table 4 and Supporting Information Figure S10, all films at low loadings of  $C_{60}$  (<5%) yield good gel percent values (>90%). Furthermore, all films prepared using the flexible monomers (TMPMP:TMPDE) yield similar gel percents, all above 90%. However, a very different trend was observed with films prepared using the rigid (PETMP:TTT) monomers with higher loadings of  $C_{60}$  (>10%), where the ene deficient PETMP:TTT-0.75 films exhibit significantly higher gel percent values (99% and 98%) compared to the PETMP:TTT-1 film series (88% and 47%).

The amount of  $C_{60}(\text{TMB-PPO})_5$  extracted during gel percent studies was also analyzed and is reported in Table 4 and Supporting Information Figure S11. In general, the amount of  $C_{60}(\text{TMB-PPO})_5$  was found to compare well with the gel percent values obtained. For all samples, an expected trend in the amount of  $C_{60}(\text{TMB-PPO})_5$  extracted increased as a function of  $C_{60}$  loading. All samples prepared with TMPMP:TMPDE monomers, as well as, the PETMP:TTT-0.75 films resulted in films with moderately low (<7%) amounts of extracted  $C_{60}(\text{TMB-PPO})_5$ . Both gel percent values and the amount of  $C_{60}(\text{TMB-PPO})_5$  extracted from the prepared films suggests that  $C_{60}$  is being covalently incorporated into the films, as observed by high gel percent values and a low amount of  $C_{60}(\text{TMB-PPO})_5$  extracted from all films except the PETMP:TTT-1 10 and 20 wt % film series, which were crumbly films of poor quality.

The thermal and mechanical properties of the resulting TE films were explored as a function of  $C_{60}$  loading, alkyl ene concentration, and monomer rigidity. Thermal stability of the resulting films was determined using TGA, and representative TGA plots are provided in Figure 5 as well as Supporting Information Figure S12. Thermal degradation onset temperatures and % char were calculated from TGA and are recorded in Table 4. For both film series, a decrease in thermal stability is observed with an increase in  $C_{60}$  loading. This is attributed to a more favorable breaking of the

fullerene-addend bond, allowing the fullerene to re-establish conjugation. Reports of increased thermal stability on polymer networks containing blended fullerene derivatives suggest that optimal stabilization occurs at low loadings of  $C_{60}$  (0.4–0.8 wt%), where higher loadings increase aggregation, thus deforming the morphological interactions between polymer chains and negatively impacting the networks [66]. Another study of the thermal stability of  $C_{60}$ -containing PS and PMMA concluded that increased thermal stability of  $C_{60}$ -containing networks occurred only with blended  $C_{60}$  due to its superior ability of the  $\pi$ -system to “trap” radicals resulting from thermal degradation, while  $C_{60}$  networks containing multiple covalent attachments to the network lacked this characteristic, thus demonstrating decreased thermal stability [77].

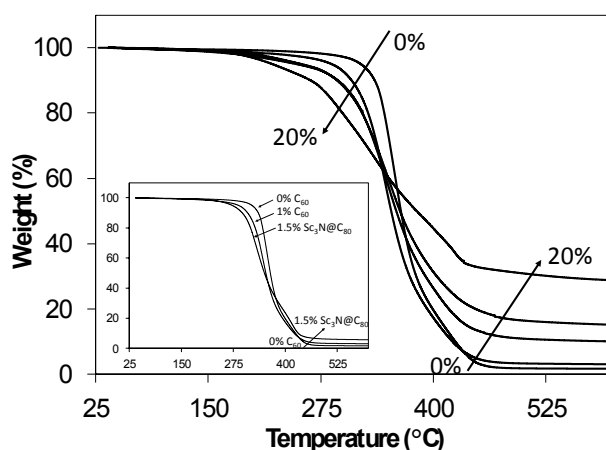


**Figure 5.** Thermal analysis of TMPMP:TMPDE-0.75 films.

All films were analyzed using DSC and obtained  $T_g$  values, along with the temperature step width of the  $T_g$ , are reported in Table 4 and graphed in Figure 6 and Supporting Information Figure 13. For the flexible films series, a general trend was observed where the  $T_g$  increases ( $\sim 28$  °C) and a broadening of step width of the  $T_g$  ( $\sim 20$  °C) was observed as a function of  $C_{60}$  loading independent of alkyl ene concentration. However, the  $T_g$  for the rigid film series was found to be depended on both  $C_{60}$  loading and alkyl ene concentration, where the  $T_g$  of the control (0%  $C_{60}$ ) PETMP:TTT films decreased significantly (25 °C) with a decrease in alkyl ene concentration. The change in  $T_g$  of the control films for the rigid system, as a function of alkyl ene concentration, suggest that small changes in the network of the PETMP:TTT films yields significant changes in  $T_g$ . Furthermore, an interesting trend is observed with the PETMP:TTT-1 film series where the  $T_g$  increases initially (4 °C) with  $C_{60}$  loading (1 wt%), then declines (51 °C) as  $C_{60}$  loading continues to increase. However, with the PETMP:TTT-0.75 film series, the  $T_g$  increases (10 °C) and remains constant ( $\pm 3$  °C) up to 20 wt% loading, at which time the  $T_g$  decreases (8 °C). Furthermore, the step width of the PETMP:TTT film series was found to only vary  $\sim 5$  °C. Another trend was observed with DSC, where the enthalpic relaxation peak is only observed for the TMPMP:TMPDE films up to 5 wt %  $C_{60}$  loading and for the rigid ene deficient control (PETMP:TTT-0.75-0) film. This phenomenon is not surprising considering enthalpy relaxation is known to decrease with increasing monomer rigidity [67]. The variations in the observed  $T_g$ , broadening of the  $T_g$  step width, and the loss of enthalpy relaxation as a function of  $C_{60}$  loading, alkyl ene concentration, and monomer rigidity, further supports the covalent incorporation

of  $C_{60}$  into the TE matrix.

Increasing  $C_{60}$  loadings resulted in higher residual mass for each loaded film, reported as % char in Table 4. This remaining mass is attributed to the high thermal stability of the  $C_{60}$  and  $Sc_3N@C_{80}$  cage [78,79]. It should be noted that the remaining mass of each sample was greater than the combined mass remaining for the control sample plus fullerene loading, which has been observed in other studies and is believed to be due to one of the following possibilities. Either strong interactions occurring between the fullerene cage and the polymer network or the initiator that requires temperatures greater than  $600\text{ }^\circ\text{C}$  to dissociate, or aggregation of the derivatives within the polymer network [61]. Since the thermal stability of the nanocomposites were negatively impacted by the addition of the fullerene adducts, it does not seem likely that the increase in % char is due to strong interaction between the fullerene adducts and polymer network.

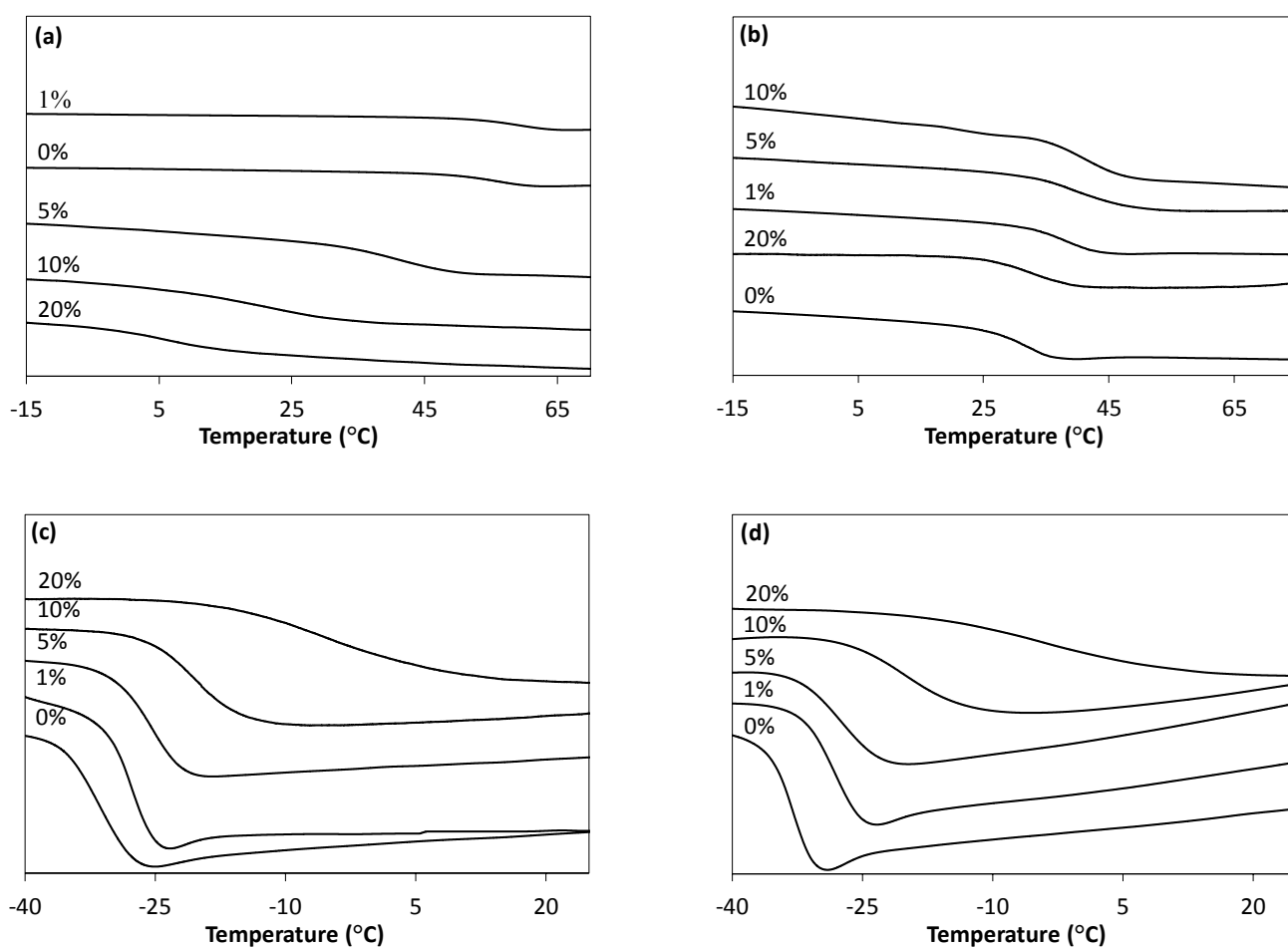


**Figure 6.** DSC plots of (a) PETMP-TTT-1, (b) PETMP:TTT-0.75, (c) TMPMP:TMPDE-1, and (d) TMPMP:TMPDE-0.75-films.

Further characterization was afforded on the prepared films to assess the dispersibility of the  $C_{60}(\text{TMB-PPO})_5$  adducts within the polymer matrix, and TEM images of the 1 and 10 wt% composites are provided in Figure 7 and Supporting Information Figures S14–S22. An interesting phenomena of larger aggregates were observed within the rigid PETMP:TTT film series; however, the fullerene containing TMPMP:TMPDE films appeared continuous throughout. The aggregation of

$C_{60}(\text{TMB-PPO})_5$  within the PETMP:TTT films could be due to increased reactivity/functionality or changes in miscibility with PETMP and TTT monomers, excluding the  $C_{60}(\text{TMB-PPO})_5$  during polymerization and resulting in phase segregation.

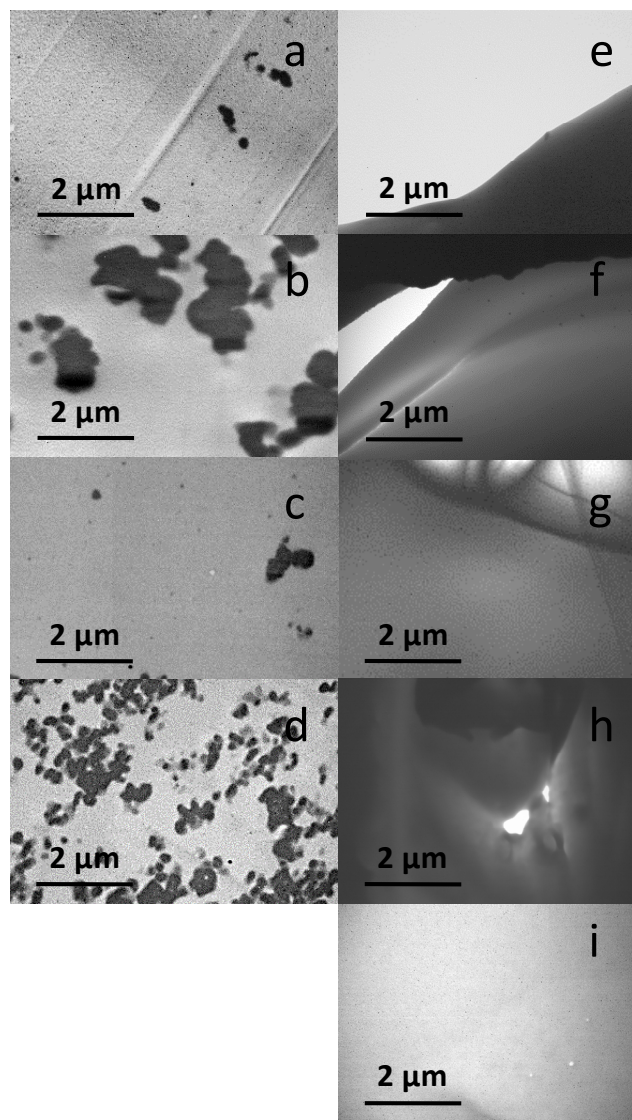


**Figure 7.** TEM images of films (a) PETMP:TTT-1-1, (b) PETMP:TTT-1-10, (c) PETMP:TTT-0.75-1, (d) PETMP:TTT-0.75-10, (e) TMPMP:TMPDE-1-1, (f) TMPMP:TMPDE-1-10, (g) TMPMP:TMPDE-0.75-1, (h) TMPMP:TMPDE-0.75-10, and (i) TMPMP:TMPDE-0.75-1.5  $\text{Sc}_3\text{N}@C_{80}$ .

Composites were evaluated for the production of singlet oxygen. Direct observation studies of singlet oxygen phosphorescence were performed on the TMPMP:TMPDE-0.75 films containing 1 and 10 wt%  $C_{60}$  and 1.5 wt%  $\text{Sc}_3\text{N}@C_{80}$  films. Thickness was adjusted to yield films of comparable transparencies, assuming that the singlet oxygen observed was produced at or near the surface of the sample, not in the bulk material. As seen in Figure 8, the emission spectrum of the fullerene containing films shows a phosphorescence peak centered at 1270 nm supporting the formation of

singlet oxygen, and in general phosphorescence increases with fullerene loading. Surprisingly, the highest phosphorescence yield correlated to the  $\text{Sc}_3\text{N}@C_{80}$  films, where crosslinking reactions may have served to adjust orbital positions to promote a more favorable energy transfer to molecular oxygen.

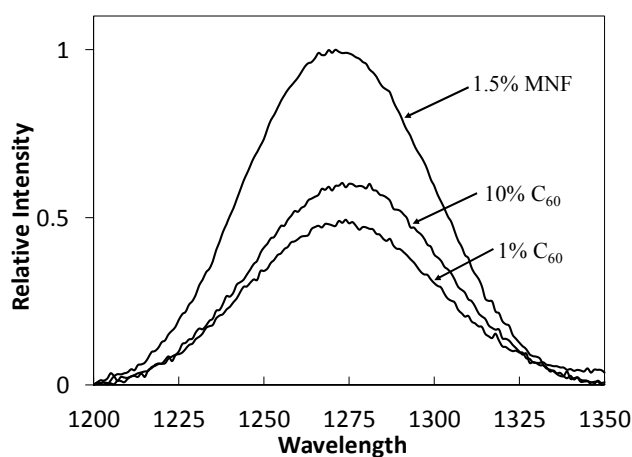


**Figure 8.** Singlet oxygen generation from TMPMP:TMPDE-0.75 fullerene containing films.

Generating singlet oxygen within a polymer matrix has the potential to degrade the network through hydrogen abstraction, scission reactions, and the oxidation of network functional groups. With the confirmed generation of singlet oxygen from the composites, a brief study was performed on the TMPMP:TMPDE-0.75 fullerene composites to characterize significant changes in the network as a function of radiation exposure time and fullerene concentration. Thin samples were cast onto salt plates and monitored before and after exposure. After irradiation, all samples, including the control sample, resulted in amber colored films. For ease of comparison, the FT-IR spectrums of  $\text{C}_{60}(\text{TMB-PPPO})_5$  containing TMPMP:TMPDE TE films are shown from 4000–2500  $\text{cm}^{-1}$  in Supporting Information Figure S24, from 1800–1550  $\text{cm}^{-1}$  in Supporting Information Figure S24; and from 1500–500  $\text{cm}^{-1}$  in Supporting Information Figure S26. Overall, relatively minor additional photodegradation is promoted at low fullerene loadings above that which is observed by the controls. A couple general statements regarding photostability and the generation of oxygenated species in the networks include (1) the growth of broad absorption bands centered around 3300  $\text{cm}^{-1}$  suggests the formation of hydroperoxide products, which increases with  $\text{C}_{60}$  loading and increased singlet oxygen production, and (2) higher loadings of  $\text{C}_{60}$  may lead to a higher fraction of unreacted enes, which are well-known reagents for reactions with singlet oxygen, the “ene” reaction. Other absorption bands yield evidence for modest increases in photodegradation at higher fullerene loadings, such as the broadening of the carbonyl stretch at 1739  $\text{cm}^{-1}$  suggesting the formation of new carbonyl moieties upon generating singlet oxygen (Supporting Information Figure S25). However, previous work by our group has demonstrated that in polymer composites bearing residual enes and readily abstractable hydrogens, the in-situ generation of singlet oxygen can be devastating to network physical properties in a very short time scale [60].

## 4. Conclusion

Chemical modification of fullerenes has been shown to greatly enhance solubility and processability of fullerenes. As a result, a library of reactions has evolved which enable the surface functionalization of fullerenes creating interesting derivatives, which are more amenable to the preparation of fullerene polymer nanocomposites. Of these, radical addition reactions continue to be an important methodology.  $C_{60}$  and  $Sc_3N@C_{80}$  derivatives were prepared via radical addition of the photodecomposition products from the commercial photoinitiator TMB-PPO, yielding  $C_{60}(TMB-PPO)_5$  and  $Sc_3N@C_{80}(TMB-PPO)_3$  as preferred soluble derivatives obtained in high yields (>95%). The solubility of  $C_{60}(TMB-PPO)_5$  was found to increase to a remarkably high value of  $\sim 260 \text{ mg mL}^{-1}$  in DMC. Further characterization of the mixture of isomers using standard techniques suggests an overall 1PPO:6TMB ratio of addends, reflecting the increased reactivity of the carbon radical. Although a higher percentage of PPO is observed in the  $Sc_3N@C_{80}(TMB-PPO)_3$  population, perhaps due to reverse electronic requirements of the substrate. Visually dispersed TE nanocomposites with low extractables were prepared using two monomer compositions of PETMP:TTT ( $T_g$  56) and TMPMP:TMPDE ( $T_g$  -32) with increasing fullerene derivative loading and at two different TE molar equivalents (1:1 or 1:0.75) to probe network structure-property relationships. The thermal and mechanical properties of the resulting TE films were explored as a function of  $C_{60}$  loading, alkyl ene concentration, and monomer rigidity. Thermal stability of the derivatives and the resulting networks was determined using TGA and was found to decrease with an increase in monomer functionality and at high fullerene loadings, respectively. Which is attributed to the favorable breaking of the fullerene-addend bond, allowing the fullerene to re-establish conjugation. All films were also analyzed using DSC and  $T_g$  values were obtained. The  $T_g$  of the flexible film series was found to increase as a function of  $C_{60}$  loading independent of alkyl ene concentration. Whereas, the  $T_g$  of the rigid film series was found to be dependent on both  $C_{60}$  loading and alkyl ene concentration. Furthermore, enthalpic relaxations observed with DSC decreased with an increase in  $C_{60}$  loading and monomer rigidity. TMPMP:TMPDE composite networks show well-dispersed derivatives via TEM imaging, and PETMP:TTT composites show phase separation in TEM, which is supported by the observed  $T_g$ 's. Singlet oxygen generation of the derivatives decreases with increased functionality; however this is compensated for by the tremendous increase in solubility in organic solvents and miscibility with monomers. Most importantly, singlet oxygen generation from the composites increased with fullerene derivative loading, with good photostability of the networks.

## Acknowledgments

Financial support for this work was provided through the NSF GK-12 Program-University of Southern Mississippi, "Connections in the Classroom: Molecules to Muscles" award #0947944, the National Science Foundation (NSF) CAREER program award #CHE-0847481, and the NSF instrumentation grant #CHE-0840390. The authors would also like to thank David Delatte and Jessica Douglas from USM for obtaining DSC data and help with TEM images, respectively. The authors would also like to thank James H. Wynne and Jeffrey G. Lundin from NRL for obtaining XPS data.

## Conflict of Interest

The authors declare no conflict of interest.

## References

1. Arbogast JW, Darmanyan AP, Foote CS, et al. (1991) Photophysical properties of sixty atom carbon molecule (C<sub>60</sub>). *J Phys Chem* 95: 11–12.
2. Ching WY, Huang MZ, Xu YN, et al. (1991) First-principles calculation of optical properties of the carbon sixty-atom molecule in the fcc. lattice. *Phys Rev Lett* 67: 2045–2048.
3. Maser W, Roth S, Anders J, et al. (1992) P-Type doping of C<sub>60</sub> fullerene films. *Synth Met* 51: 103–108.
4. Sun Y-P, Lawson GE, Riggs JE, et al. (1998) Photophysical and Nonlinear Optical Properties of [60]Fullerene Derivatives. *J Phys Chem A* 102: 5520–5528.
5. Accorsi G, Armaroli N (2010) Taking Advantage of the Electronic Excited States of [60]-Fullerenes. *J Phys Chem C* 114: 1385–1403.
6. Allemand PM, Khemani KC, Koch A, et al. (1991) Organic molecular soft ferromagnetism in a fullerene C<sub>60</sub>. *Science* 253: 301–303.
7. Stephens PW, Cox D, Lauher JW, et al. (1992) Lattice structure of the fullerene ferromagnet TDAE-C<sub>60</sub>. *Nature* 355: 331–332.
8. Hebard AF, Rosseinsky MJ, Haddon RC, et al. (1991) Superconductivity at 18 K in potassium-doped fullerene (C<sub>60</sub>). *Nature* 350: 600–601.
9. Dubois D, Moninot G, Kutner W, et al. (1992) Electroreduction of Buckminsterfullerene, C<sub>60</sub>, in aprotic solvents. Solvent, supporting electrolyte, and temperature effects. *J Phys Chem* 96: 7137–7145.
10. Schon TB, Di Carmine PM, Seferos DS (2014) Polyfullerene Electrodes for High Power Supercapacitors. *Adv Energy Mater* 4: 1301509–1301515.
11. Pupysheva OV, Farajian AA, Yakobson BI (2008) Fullerene Nanocage Capacity for Hydrogen Storage. *Nano Lett* 8: 767–774.
12. Nadtochenko VA, Vasil'ev IV, Denisov NN, et al. (1993) Photophysical properties of fullerene C<sub>60</sub>: picosecond study of intersystem crossing. *J Photochem Photobiol, A* 70: 153–156.
13. Foote CS (1994) Photophysical and photochemical properties of fullerenes. *Electron Transfer I*. Berlin, Heidelberg: Springer Berlin Heidelberg. pp. 347–363.
14. Sun R, Jin C, Zhang X, et al. (1994) Photophysical properties of C<sub>60</sub>. *Wuli* 23: 83–87.
15. Qu B, Chen SM, Dai LM (2000) Simulation analysis of ESR spectrum of polymer alkyl-C<sub>60</sub> radicals formed by photoinitiated reactions of low-density polyethylene. *Appl Magn Reson* 19: 59–67.
16. Guldi DM, Asmus K-D (1997) Photophysical Properties of Mono- and Multiply-Functionalized Fullerene Derivatives. *J Phys Chem A* 101: 1472–1481.
17. McEwen CN, McKay RG, Larsen BS (1992) C<sub>60</sub> as a radical sponge. *J Am Chem Soc* 114: 4412–4414.
18. Tzirakis MD, Orfanopoulos M (2013) Radical Reactions of Fullerenes: From Synthetic Organic Chemistry to Materials Science and Biology. *Chem Rev* 113: 5262–5321.
19. Krusic PJ, Wasserman E, Keizer PN, et al. (1991) Radical reactions of C<sub>60</sub>. *Science* 254:

- 1183–1185.
20. Krusic PJ, Wasserman E, Parkinson BA, et al. (1991) Electron spin resonance study of the radical reactivity of C<sub>60</sub>. *J Am Chem Soc* 113: 6274–6275.
  21. Wu S-H, Sun W-Q, Zhang D-W, et al. (1998) Reaction of [60]fullerene with trialkylphosphine oxide. *Tetrahedron Lett* 39: 9233–9236.
  22. Cheng F, Yang X, Fan C, et al. (2001) Organophosphorus chemistry of fullerene: synthesis and biological effects of organophosphorus compounds of C<sub>60</sub>. *Tetrahedron* 57: 7331–7335.
  23. Cheng F, Yang X, Zhu H, et al. (2000) Synthesis and optical properties of tetraethyl methano[60]fullerenediphosphonate. *Tetrahedron Lett* 41: 3947–3950.
  24. Liu Z-B, Tian J-G, Zang W-P, et al. (2003) Large optical nonlinearities of new organophosphorus fullerene derivatives. *Appl Opt* 42: 7072–7076.
  25. Ford WT, Nishioka T, Qiu F, et al. (1999) Structure Determination and Electrochemistry of Products from the Radical Reaction of C<sub>60</sub> with Azo(bis(isobutyronitrile)). *J Org Chem* 64: 6257–6262.
  26. Ford WT, Nishioka T, Qiu F, et al. (2000) Dimethyl Azo(bis(isobutyrate)) and C<sub>60</sub> Produce 1,4- and 1,16-Di(2-carbomethoxy-2-propyl)-1,x-dihydro[60]fullerenes. *J Org Chem* 65: 5780–5784.
  27. Shustova NB, Peryshkov DV, Kuvychko IV, et al. (2011) Poly(perfluoroalkylation) of Metallic Nitride Fullerenes Reveals Addition-Pattern Guidelines: Synthesis and Characterization of a Family of Sc<sub>3</sub>N@C<sub>80</sub>(CF<sub>3</sub>)<sub>n</sub> (n = 2-16) and Their Radical Anions. *J Am Chem Soc* 133: 2672–2690.
  28. Shu C, Slebodnick C, Xu L, et al. (2008) Highly Regioselective Derivatization of Trimetallic Nitride Templated Endohedral Metallofullerenes via a Facile Photochemical Reaction. *J Am Chem Soc* 130: 17755–17760.
  29. Shu C, Cai T, Xu L, et al. (2007) Manganese(III)-Catalyzed Free Radical Reactions on Trimetallic Nitride Endohedral Metallofullerenes. *J Am Chem Soc* 129: 15710–15717.
  30. Shustova NB, Popov AA, Mackey MA, et al. (2007) Radical Trifluoromethylation of Sc<sub>3</sub>N@C<sub>80</sub>. *J Am Chem Soc* 129: 11676–11677.
  31. Cardona CM, Kitaygorodskiy A, Echegoyen L (2005) Trimetallic nitride endohedral metallofullerenes: Reactivity dictated by the encapsulated metal cluster. *J Am Chem Soc* 127: 10448–10453.
  32. Yu G, Gao J, Hummelen JC, et al. (1995) Polymer photovoltaic cells: enhanced efficiencies via a network of internal donor-acceptor heterojunctions. *Science* 270: 1789–1791.
  33. Troshin PA, Hoppe H, Renz J, et al. (2009) Material Solubility-Photovoltaic Performance Relationship in the Design of Novel Fullerene Derivatives for Bulk Heterojunction Solar Cells. *Adv Funct Mater* 19: 779–788.
  34. Jiao F, Liu Y, Qu Y, et al. (2010) Studies on anti-tumor and antimetastatic activities of fulleranol in a mouse breast cancer model. *Carbon* 48: 2231–2243.
  35. Xu J-Y, Su Y-Y, Cheng J-S, et al. (2010) Protective effects of fulleranol on carbon tetrachloride-induced acute hepatotoxicity and nephrotoxicity in rats. *Carbon* 48: 1388–1396.
  36. Mikawa M, Kato H, Okumura M, et al. (2001) Paramagnetic Water-Soluble Metallofullerenes Having the Highest Relaxivity for MRI Contrast Agents. *Bioconjugate Chem* 12: 510–514.
  37. Chen C, Xing G, Wang J, et al. (2005) Multihydroxylated [Gd@C<sub>82</sub>(OH)<sub>22</sub>]<sub>n</sub> Nanoparticles: Antineoplastic Activity of High Efficiency and Low Toxicity. *Nano Lett* 5: 2050–2057.
  38. Aoshima H, Kokubo K, Shirakawa S, et al. (2009) Antimicrobial activity of fullerenes and their

- hydroxylated derivatives. *Biocontrol Sci* 14: 69–72.
39. Guldi DM, Asmus K-D (1999) Activity of water-soluble fullerenes towards  $\cdot\text{OH}$ -radicals and molecular oxygen. *Radiat Phys Chem* 56: 449–456.
  40. Lai HS, Chen WJ, Chiang LY (2000) Free radical scavenging activity of fulleranol on the ischemia-reperfusion intestine in dogs. *World J Surg* 24: 450–454.
  41. Sun D, Zhu Y, Liu Z, et al. (1997) Active oxygen radical scavenging ability of water-soluble fullerenols. *Chin Sci Bull* 42: 748–752.
  42. Dugan LL, Gabrielsen JK, Yu SP, et al. (1996) Buckminsterfullerenol free radical scavengers reduce excitotoxic and apoptotic death of cultured cortical neurons. *Neurobiol Dis* 3: 129–135.
  43. Chiang LY, Lu F-J, Lin J-T (1995) Free radical scavenging activity of water-soluble fullerenols. *J Chem Soc, Chem Commun*: 1283–1284.
  44. Xiao L, Takada H, Maeda K, et al. (2005) Antioxidant effects of water-soluble fullerene derivatives against ultraviolet ray or peroxy lipid through their action of scavenging the reactive oxygen species in human skin keratinocytes. *Biomed Pharmacother* 59: 351–358.
  45. Oberdorster E (2004) Manufactured nanomaterials (fullerenes, C60) induce oxidative stress in the brain of juvenile largemouth bass. *Environ Health Perspect* 112: 1058–1062.
  46. Hamano T, Okuda K, Mashino T, et al. (1997) Singlet oxygen production from fullerene derivatives: effect of sequential functionalization of the fullerene core. *Chem Commun* 21–22.
  47. Guldi DM, Prato M (2000) Excited-State Properties of C60 Fullerene Derivatives. *Acc Chem Res* 33: 695–703.
  48. Jensen AW, Daniels C (2003) Fullerene-Coated Beads as Reusable Catalysts. *J Org Chem* 68: 207–210.
  49. Jensen AW, Maru BS, Zhang X, et al. (2005) Preparation of fullerene-shell dendrimer-core nanoconjugates. *Nano Lett* 5: 1171–1173.
  50. Foote CS (1994) Photophysical and photochemical properties of fullerenes. *Top Curr Chem* 169: 347–363.
  51. McCluskey DM, Smith TN, Madasu PK, et al. (2009) Evidence for Singlet-Oxygen Generation and Biocidal Activity in Photoresponsive Metallic Nitride Fullerene-Polymer Adhesive Films. *ACS Appl Mater Interfaces* 1: 882–887.
  52. Alberti MN, Orfanopoulos M (2010) Recent mechanistic insights in the singlet oxygen ene reaction. *Synlett* 999–1026.
  53. Foote CS, Wexler S, Ando W (1965) Singlet oxygen. III. Product selectivity. *Tetrahedron Lett* 4111–4118.
  54. Dallas P, Rogers G, Reid B, et al. (2016) Charge separated states and singlet oxygen generation of mono and bis adducts of C60 and C70. *Chem Phys* 465–466: 28–39.
  55. Yano S, Naemura M, Toshimitsu A, et al. (2015) Efficient singlet oxygen generation from sugar pendant C60 derivatives for photodynamic therapy [Erratum to document cited in CA163:618143]. *Chem Commun* 51: 17631–17632.
  56. Prat F, Stackow R, Bernstein R, et al. (1999) Triplet-State Properties and Singlet Oxygen Generation in a Homologous Series of Functionalized Fullerene Derivatives. *J Phys Chem A* 103: 7230–7235.
  57. Tegos GP, Demidova TN, Arcila-Lopez D, et al. (2005) Cationic Fullerenes Are Effective and Selective Antimicrobial Photosensitizers. *Chem Biol* 12: 1127–1135.
  58. Schinazi RF, Sijbesma R, Srdanov G, et al. (1993) Synthesis and virucidal activity of a

- water-soluble, configurationally stable, derivatized C60 fullerene. *Antimicrob Agents Chemother* 37: 1707–1710.
59. Dai L (1999) Advanced syntheses and microfabrications of conjugated polymers, C60-containing polymers and carbon nanotubes for optoelectronic applications. *Polym Adv Technol* 10: 357–420.
60. Phillips JP, Deng X, Todd ML, et al. (2008) Singlet oxygen generation and adhesive loss in stimuli-responsive, fullerene-polymer blends, containing polystyrene-block-polybutadiene-block-polystyrene and polystyrene-block-polyisoprene-block-polystyrene rubber-based adhesives. *J Appl Polym Sci* 109: 2895–2904.
61. Lundin JG, Giles SL, Cozzens RF, et al. (2014) Self-cleaning photocatalytic polyurethane coatings containing modified C60 fullerene additives. *Coatings* 4: 614–629.
62. Phillips JP, Deng X, Stephen RR, et al. (2007) Nano- and bulk-tack adhesive properties of stimuli-responsive, fullerene-polymer blends, containing polystyrene-block-polybutadiene-block-polystyrene and polystyrene-block-polyisoprene-block-polystyrene rubber-based adhesives. *Polymer* 48: 6773–6781.
63. Samulski ET, DeSimone JM, Hunt MO, Jr., et al. (1992) Flagellenes: nanophase-separated, polymer-substituted fullerenes. *Chem Mater* 4: 1153–1157.
64. Chiang LY, Wang LY, Kuo C-S (1995) Polyhydroxylated C60 Cross-Linked Polyurethanes. *Macromolecules* 28: 7574–7576.
65. Ahmed HM, Hassan MK, Mauritz KA, et al. (2014) Dielectric properties of C60 and Sc<sub>3</sub>N@C80 fullerenol containing polyurethane nanocomposites. *J Appl Polym Sci* 131: 40577–40588.
66. Kokubo K, Takahashi R, Kato M, et al. (2014) Thermal and thermo-oxidative stability of thermoplastic polymer nanocomposites with arylated [60]fullerene derivatives. *Polym Compos*: 1–9.
67. Shin J, Nazarenko S, Phillips JP, et al. (2009) Physical and chemical modifications of thiol-ene networks to control activation energy of enthalpy relaxation. *Polymer* 50: 6281–6286.
68. Hoyle CE, Bowman CN (2010) Thiol-ene click chemistry. *Angew Chem Int Ed* 49: 1540–1573.
69. Hoyle CE, Lee TY, Roper T (2004) Thiol-enes: Chemistry of the past with promise for the future. *J Polym Sci A Polym Chem* 42: 5301–5338.
70. Cramer NB, Scott JP, Bowman CN (2002) Photopolymerizations of Thiol-Ene Polymers without Photoinitiators. *Macromolecules* 35: 5361–5365.
71. Li Q, Zhou H, Hoyle CE (2009) The effect of thiol and ene structures on thiol-ene networks: Photopolymerization, physical, mechanical and optical properties. *Polymer* 50: 2237–2245.
72. Northrop BH, Coffey RN (2012) Thiol-Ene Click Chemistry: Computational and Kinetic Analysis of the Influence of Alkene Functionality. *J Am Chem Soc* 134: 13804–13817.
73. Singh R, Goswami T (2011) Understanding of thermo-gravimetric analysis to calculate number of addends in multifunctional hemi-ortho ester derivatives of fullerenol. *Thermochimica Acta* 513: 60–67.
74. Barker EM, Buchanan JP (2016) Thiol-ene polymer microbeads prepared under high-shear and their successful utility as a heterogeneous photocatalyst via C60-capping. *Polymer* 92: 66–73.
75. Jockusch S, Turro NJ (1998) Phosphinoyl Radicals: Structure and Reactivity. A Laser Flash Photolysis and Time-Resolved ESR Investigation. *J Am Chem Soc* 120: 11773–11777.
76. Ruoff RS, Tse DS, Malhotra R, et al. (1993) Solubility of fullerene (C60) in a variety of solvents. *J Phys Chem* 97: 3379–3383.
77. Ginzburg BM, Shibaev LA, Melenevskaja EY, et al. (2004) Thermal and Tribological Properties

of Fullerene-Containing Composite Systems. Part 1. Thermal Stability of Fullerene-Polymer Systems. *J Macromol Sci Phys* 43: 1193–1230.

78. Leifer SD, Goodwin DG, Anderson MS, et al. (1995) Thermal decomposition of a fullerene mix. *Phys Rev B Condens Matter* 51: 9973–9981.
79. Mackey MA (2011) Exploration in metallic nitride fullerenes and oxometallic fullerenes: A new class of metallofullerenes [Ph.D. Dissertation]. Hattiesburg, MS: The University of Southern Mississippi.



**AIMS Press**

© 2016 Janice Paige Buchanan, et al., licensee AIMS Press. This is an open access article distributed under the terms of the Creative Commons Attribution License (<http://creativecommons.org/licenses/by/4.0>)